Monthly Notices
of the
ROYAL ASTRONOMICAL SOCIETY

MNRAS **525,** 4042–4056 (2023)
https://doi.org/10.1093/mnras/stad2531
Advance Access publication 2023 September 4

Late-time *HST* UV and optical observations of AT 2018cow: extracting a cow from its background

Anne Inkenhaag [1,2]★ Peter G. Jonker,[1,2] Andrew J. Levan,[1,3] Ashley A. Chrimes [1]
Andrew Mummery,[4] Daniel A. Perley [5] and Nial R. Tanvir[6]

[1] *Department of Astrophysics/IMAPP, Radboud University Nijmegen, P.O. Box 9010, NL-6500 GL Nijmegen, the Netherlands*
[2] *SRON, Netherlands Institute for Space Research, Niels Bohrweg 4, NL-2333 CA Leiden, the Netherlands*
[3] *Department of Physics, University of Warwick, Gibbet Hill Road, Coventry CV4 7AL, UK*
[4] *Oxford Astrophysics, Denys Wilkinson Building, Keble Road, Oxford OX1 3RH, UK*
[5] *Astrophysics Research Institute, Liverpool John Moores University, IC2, Liverpool Science Park, 146 Brownlow Hill, Liverpool L3 5RF, UK*
[6] *School of Physics and Astronomy, University of Leicester, University Road, Leicester LE1 7RH, UK*

Accepted 2023 August 11. Received 2023 August 4; in original form 2023 May 16

ABSTRACT

The bright, blue, rapidly evolving AT 2018cow is a well-studied peculiar extragalactic transient. Despite an abundance of multiwavelength data, there still is no consensus on the nature of the event. We present our analysis of three epochs of *Hubble Space Telescope (HST)* observations spanning the period from 713 to 1474 d post-burst, paying particular attention to uncertainties of the transient photometry introduced by the complex background in which AT 2018cow resides. Photometric measurements show evident fading in the UV and more subtle but significant fading in the optical. During the last *HST* observation, the transient's optical/UV colours were still bluer than those of the substantial population of compact, young, star-forming regions in the host of AT 2018cow, suggesting some continued transient contribution to the light. However, a compact source underlying the transient would substantially modify the resulting spectral energy distribution, depending on its contribution in the various bands. In particular, in the optical filters, the complex, diffuse background poses a problem for precise photometry. An underlying cluster is expected for a supernova occurring within a young stellar environment or a tidal-disruption event (TDE) within a dense older one. While many recent works have focused on the supernova interpretation, we note the substantial similarity in UV light-curve morphology between AT 2018cow and several tidal disruption events around supermassive black holes. Assuming AT 2018cow arises from a TDE-like event, we fit the late-time emission with a disc model and find $M_{\rm BH} = 10^{3.2 \pm 0.8}$ M$_{\odot}$. Further observations are necessary to determine the late-time evolution of the transient and its immediate environment.

Key words: stars: individual: AT 2018cow – supernovae: general – ultraviolet: stars – transients: supernovae – transients: tidal disruption events.

1 INTRODUCTION

Multiwavelength, wide field-of-view surveys at various wavelengths have transformed transient astrophysics. From X-rays with *Swift* (Burrows et al. 2005) and *eROSITA* (Predehl et al. 2021) through to optical with e.g. the Zwicky Transient Facility (ZTF); Bellm et al. (2019), the All-Sky Automated Survey for Supernovae (ASASSN)[1]; (Shappee et al. 2014), and the Asteroid Terrestrial-Impact Last Alert System (ATLAS); (Tonry 2011), and radio surveys [e.g. the VLA sky survey Lacy et al. 2020, the Canadian Hydrogen Intensity Mapping Experiment (CHIME); CHIME Collaboration (2022), and MeerKAT; Jonas & MeerKAT Team (2016)], we can now identify and follow hundreds to thousands of transients, such as gamma-ray bursts (GRBs), supernovae (SNe), and fast radio bursts (FRBs), per year. These high rates result from the combination of areal coverage, depth and cadence of these surveys, and the intrinsic volumetric rate and luminosity function of the transients under consideration. Due to these large, high cadence, sensitive surveys, events that are intrinsically rare, or that are numerous but faint, are also being detected. At the extremes of parameter space, we detect events whose nature stretches plausible progenitor models. These events are thus extremely valuable for study in their own right.

One class of such peculiar transients are fast blue optical transients (FBOTs; e.g. Drout et al. 2014; Arcavi et al. 2016; Whitesides et al. 2017; Pursiainen et al. 2018; Tampo et al. 2020; Ho et al. 2023). A handful of FBOTs have been discovered over the last decade: CSS161010 (Coppejans et al. 2020), AT2018lug/ZTF18abvkwla (Ho et al. 2020), AT2020xnd/ZTF20acigmel (Perley et al. 2021), AT2020mrf (Yao et al. 2022), and the well-known example AT 2018cow (Prentice et al. 2018; Perley et al. 2019). Together, these events form their own class of astrophysical transients, although the FBOT properties are heterogeneous, and the nature of the events is still uncertain. This class of events is characterized by fast rise and decay times, high peak luminosities (absolute peak magnitude $\lesssim -19$), and early spectra dominated by a blue featureless continuum. Multiple models were suggested, such as peculiar supernovae (SNe)

★ E-mail: a.inkenhaag@astro.ru.nl

[1] https://www.astronomy.ohio-state.edu/asassn/

and magnetars formed in double neutron star mergers (Drout et al. 2014). In SNe the time-scale of Ni^{56} radioactive decay and the diffusion time-scale are critical parameters in the light-curve evolution (Arnett 1982). However, these two time-scales are too long to explain the rapid decay and high peak luminosity observed for FBOTs (Drout et al. 2014; Pursiainen et al. 2018).

AT 2018cow was the first FBOT discovered in real-time instead of archival searches. The transient rose to peak rapidly (>5 mag in ∼3.5 d), was extremely bright ($L_{\rm peak} \approx 10^{44}$ erg s^{-1}; Prentice et al. 2018; Perley et al. 2019) and was detected across the electromagnetic (EM) spectrum. The host galaxy CGCG137−068 has a luminosity distance of 63.0 ± 4.4 Mpc (redshift $z = 0.01404 \pm 0.00002$) (SDSS DR6; Adelman-McCarthy et al. 2008). The combination of high (peak) luminosity and relatively low distance meant that many telescopes and satellites could observe and detect it, and led to an extensive observational campaign.

Observations of AT 2018cow showed that the luminosity decay was too fast to be powered by Ni^{56} decay (Margutti et al. 2019). In addition, the photospheric radius stayed hot and small for hundreds of days (Perley et al. 2019; Sun et al. 2022). The optical spectra were featureless the first ∼20 d; after that period, emission lines of hydrogen and helium appeared (Prentice et al. 2018; Margutti et al. 2019; Perley et al. 2019). The spectral evolution has some resemblance to the spectral development of SNe Ibn and IIn (Fox & Smith 2019; Xiang et al. 2021) although the lines in AT 2018cow appeared later than usual for those supernovae. The X-ray luminosity was high (e.g. Kuin et al. 2019; Margutti et al. 2019) and showed suggestive evidence for the presence of one or more quasi-periodic oscillations (QPOs) (Pasham et al. 2021; Zhang et al. 2022). QPOs are regularly seen in accreting systems, and the combination of a high luminosity and the detection of a QPO, if real, would thus suggest AT 2018cow is caused by an accreting compact object.

The host galaxy of AT 2018cow appears to be a face on spiral system, and there are several (at least two) star-forming regions that lie close to (within ∼400 parsec of) the (projected) position of AT 2018cow. Assuming AT 2018cow lies in the plane of the host galaxy and not above or below it, this provides suggestive evidence for a link between massive star evolutionary processes and AT 2018cow (Morokuma-Matsui et al. 2019; Lyman et al. 2020). On the other hand, Sun et al. (2023) suggest that the low extinction in the transient implies that it is more likely on the near side of the disc and is not necessarily embedded in the star-forming regions. It would argue against a link with a massive star progenitor if this is correct.

Combining all the observed properties, the emission of AT 2018cow most likely comes from an engine-driven explosion (e.g. Margutti et al. 2019; Perley et al. 2019). Multiple models have been proposed for AT 2018cow (and FBOTs in general), including magnetars (Prentice et al. 2018; Mohan, An & Yang 2020; Liu et al. 2022), interactions with the circumstellar material (Rivera Sandoval et al. 2018; Pellegrino et al. 2022) and a pre-existing stellar mass BH disrupting or accreting a companion (Metzger 2022). Among the proposed models, the following two are considered most promising: An engine-powered core-collapse event, where a compact object is formed that accretes progenitor material (Prentice et al. 2018; Margutti et al. 2019; Perley et al. 2019; Mohan et al. 2020), or a tidal disruption event (TDE) of a white dwarf (WD) or main sequence (MS) star by an intermediate mass black hole (IMBH; Kuin et al. 2019; Perley et al. 2019). This class of TDEs may naturally explain the fainter and faster evolution compared to classical TDEs [of stars by a supermassive black hole (SMBH)], as well as provide an explanation for the non-nuclear location of the transient (Maguire et al. 2020). However, the IMBH must reside in a dense stellar environment such that two-body relaxation is efficient enough to scatter a WD (or MS star) into the tidal radius within a Hubble time. Such a dense stellar environment is then a requirement for the TDE interpretation to be viable, although previous research does not provide evidence for such an environment (e.g. Margutti et al. 2019). However, long-lived, luminous emission from AT 2018cow makes detecting any putative (underlying) stellar cluster difficult.

The *Hubble Space Telescope (HST)* observed AT 2018cow several times over the 4-yr period since its first detection. Surprisingly, Sun et al. (2022, 2023) detected UV-radiation even more than 4 yr after the first detection of AT 2018cow. This emission is consistent with a hot and bright source and Sun et al. (2022) suggest a massive star progenitor is most likely involved.

In this work, we present our analysis of the late-time *HST* data of AT 2018cow, spanning three epochs between 713 and 1474 d after the initial detection. The filters range from F225W in the UV to F814W in the red part of the optical. We perform photometry in multiple ways and investigate the influence of the background measurement on the photometry outcome. We also investigate whether the detected emission is from AT 2018cow itself or the environment and if there are implications from this distinction for the progenitor scenarios. We investigate if the UV properties can be explained under a TDE scenario and what the implications would be.

All magnitudes are presented in the AB magnitude system unless specified otherwise. Throughout the paper we use $H_0 = 67.8\,\mathrm{km\,s^{-1}\,Mpc^{-1}}$, $\Omega_{\rm m} = 0.308$, and $\Omega_\Lambda = 0.692$ (Planck Collaboration XIII 2016).

2 DATA ANALYSIS

For this work we use observations of AT 2018cow by *HST* using the ultraviolet–visible (UVIS) channel of the Wide Field Camera 3 (WFC3) at three different late-time epochs. The data we use were taken under programme IDs 15974, 16 179, and 16 925 with PIs A. Levan, A. Filippenko, and Y. Chen, respectively. The observations are taken 713, 1135, and 1474 d after the first detection of the transient, which we take to be $T_0 = 58285.44$ (Perley et al. 2019). We obtain the individual on-the-fly processed images from the Mikulski Archive for Space Telescopes,[2] these have had flat field and bias corrections applied and have also been corrected for the impact of charge transfer efficiency on the ageing WFC3 CCDs.

2.1 Alignment

First we combine the individual images using ASTRODRIZZLE from the python package DRIZZLEPACK (Hoffmann, Mack & et al. 2021).[3]Here, we set the final pixel scale to `final_scale = 0.025` to utilize subpixel dithering to obtain more finely sampled images and to better sample the *HST* point spread function (PSF). We use default settings for parameters unless mentioned otherwise. Next, we use the GEOMAP task in IRAF (Tody 1986, 1993) to align the images obtained in the four different filters 713 d after the onset. The sources used for this alignment are the galaxy nucleus {R.A., Dec} = {16:16:00.582,+22:16:08.286} and a star {R.A., Dec} = {16:15:59.147, +22:15:58.88}: both are detected in all four filters. After this, we use XREGISTER to align each filter image obtained at the one (F225W and F336W) or two (F555W and F814W) other epoch(s) to their respective image obtained 713 d after

---

[2] https://archive.stsci.edu/

[3] https://drizzlepac.readthedocs.io/en/latest/astrodrizzle.html

the transient's first detection. We cannot use XREGISTER to align all images across all filters because it uses cross-correlation to calculate a shift, which does not work well if there are many sources that are not detected in both images, which is the case here when using observations obtained in different filters. The alignment shifts from GEOMAP and XREGISTER are used to redrizzle the images with an additional shift so the sources align pixel wise in the final images.

2.2 Aperture photometry

We perform aperture photometry using a circle with a radius of 0.08 arcsec on all the images using dual-image mode in SOURCE EXTRACTOR (Bertin & Arnouts 1996), except our detection image, F336W at $T = 713$ d, for which we use single image mode. In dual-image mode source detection is done on one image and the measurements are done on the second image. This enforces the use of a fixed position of the aperture across the different filter images. Using dual-image mode prevent us from having to cross-match the detected sources between images and forces SOURCE EXTRACTOR to perform photometry at the position of AT 2018cow. The choice of aperture radius (corresponding to a diameter of $\sim$2 times the full width at half-maximum (FWHM) ensures we measure most of the emission from AT 2018cow without measuring too much background.

We use the drizzled F336W image at epoch 713 d as our source detection image, because there clearly is still emission at the transient location, and more sources are detected in the F336W than in the F225W image. For the photometry we use default values as mentioned in the SOURCE EXTRACTOR manual[4] for parameters not mentioned here and adjust parameters such as the FWHM and pixel scale (0.08 arcsec and 0.025 arcsec pixel^{-1}, respectively). We set the detection and analysis thresholds to 3.0σ to balance between minimizing contamination from spurious detections of hot pixels and allowing the detection of faint sources in the final output. We subtract the local background from the transient light in the final photometry.

Since the individual images are shifted with respect to each other because of drizzling, certain features such as bad pixels or pixels with cosmic rays removed can influence the quality of the signal in multiple pixels in the final combined image (i.e. the noise in the final pixels is correlated to some degree). This can influence the final photometry, which we take into account by using a weight map (`WEIGHT_TYPE = MAP_WEIGHT`) in SOURCE EXTRACTOR. This weight map tells SOURCE EXTRACTOR which redrizzled pixels contain bad pixels from the individual images, which improves source detection and error estimation, see the SOURCE EXTRACTOR user manual for full details. We use the weight map that is produced by ASTRODRIZZLE during the combination process.

Aperture corrections are done using appropriate values from the table provided on the WFC3 handbook website[5] using $r = 0.08$ arcsec values in the UVIS2 table. For comparison to Sun et al. (2022), we report Vega magnitudes based on the zeropoints from the WFC3 instrument handbook.[6] Photometry is corrected for Galactic foreground reddening following Schlafly & Finkbeiner (2011).

2.3 PSF photometry

We also perform PSF photometry to examine whether the source is point-like or extended. We start by cutting out an image (17 by 17 pixels) away from the host galaxy containing an isolated point source (centred on $\{\mathrm{RA, Dec}\} = \{16{:}15{:}59.254, +22{:}1621.733\}$ for F555W and F814W, and $\{\mathrm{RA, Dec}\} = \{16{:}15{:}59.148, +22{:}15{:}58.379\}$ for F225W and F335W). This point source is used to provide an estimate of the PSF. Although it does not have as high a signal-to-noise ratio as the computed PSFs available, the advantage of this approach is that it measures the PSF directly on the image. Since the star is much brighter than the transient, the impact of photometric noise on the template PSF is minimal.

We now proceed to measure the magnitude of a point source at the location of AT 2018cow within our images. We linearly interpolate the template PSF to enable sub-pixel centroiding, confirm this model subtracts out cleanly from the PSF star image, and then perform a fit using the pixels with a central position <6.1 pixels from the best fitting (x,y) position determined before. This best-fitting position of AT 2018cow is obtained using a 4-parameter fit on the F225 image at $T = 1474$ d (the highest signal-to-noise value of the four UV images), in which the (x,y) position, the PSF normalization, and the background are left free to vary. The best-fitting (x,y) coordinates are then used as fixed input parameters for the fits on the other images (which is possible because of the pixel-wise alignment described in Section 2.1), leaving a 2-parameter fit (the normalization and background are the remaining free parameters). We minimize the χ^2 in this area and report the values for the best-fitting background and PSF normalization.

To produce PSF subtracted images, the PSF template multiplied by the best-fitting normalization is subtracted from the data at the best-fitting position. To calculate the magnitude of the subtracted point source, we sum the number of electrons/s in the template PSF in a circular area with a 6-pixel radius around the peak of the PSF, and multiply by the best-fitting normalization. We determine the error on the best-fitting peak height by performing a two parameter χ^2 fit, leaving the centroid position fixed on the best-fitting position allowing only the PSF normalization and the background to vary. The error on the height is determined using $\Delta\chi^2 = 2.30$. We calculate the error on the magnitude by multiplying the summed PSF model with the error on the PSF normalization.

We also perform PSF photometry using DOLPHOT (v2.0; Dolphin 2000). This software package is specifically designed for PSF photometry in crowded fields. It performs photometry on the individual _FLC images and combines the individual measurements into a final (Vega) magnitude for each source. We transform the Vega magnitudes into AB magnitudes using the same difference in zeropoints as mentioned in Section 2.2. We use TWEAKREG from DRIZZLEPAC to align all _FLC images to the drizzled F336W $T = 713$ d image, as this has the sharpest PSF. We then perform PSF photometry for this epoch leaving DOLPHOT free to search for sources and use the output positions of this run as fixed positions for the other filters and epochs using the 'warmstart' option in DOLPHOT.

2.4 Aperture photometry on difference images

We compute difference images using HOTPANTS (v5.1.11; Becker 2015) by subtracting epoch 3 from epoch 1 or 2 to investigate the brightness of any residual emission at the position of AT 2018cow. To perform the subtraction we use default values for the input parameters of HOTPANTS except for bgo, ko, and the nsx and nsy parameters where we use values of 0.1, 0.05, 5, and 5, respectively. The

---

[4] https://sextractor.readthedocs.io/en/latest/index.html

[5] https://www.stsci.edu/hst/instrumentation/wfc3/data-analysis/photometric-calibration/uvis-encircled-energy

[6] https://www.stsci.edu/hst/instrumentation/wfc3/data-analysis/photometric-calibration/uvis-photometric-calibration

parameters (bgo, ko, nsx, nsy) are the spatial orders of the background and kernel variations and the number of stamps within a region in x and y direction, respectively. We also change the gain (which is equal to the exposure time for the *HST* reduced data), and values for the upper and the lower valid data counts for each combination of images we compute a difference image for. We maximize the size of the difference image which is however limited by the need to avoid gaps between the CCDs in the different exposures. We also perform aperture photometry on these difference images in all filters, using the procedure described below.

We measure the flux density of any residual on the difference images by determining the number of electrons/s in a circular aperture of 0.08 arcsec radius centred on the position of AT 2018cow. From this, we subtract the mean background and we convert to magnitudes. To determine the mean and standard deviation of the background flux density in the difference images, we randomly place circular apertures of the same radius as above within 30 pixels of the position of AT 2018cow. In placing these apertures we avoid regions where in the images bright objects are present (see Fig. A1 for an example of the placement of these regions in the epoch 1 F555W image). We find a large spread in the value of the background (between a factor ∼13 and ∼1825 for the optical filters and between a factor ∼25 and ∼78 for the UV filters in the difference images and on average a factor ∼1.5 for the optical filters and between a factor ∼4 and ∼217 for the UV filters in the non-subtracted images), and therefore the magnitude and its uncertainty depend on the flux density in the background. We will come back to this in the Discussion, while in the paper we use the median background to determine the source magnitude in the difference image and the standard deviation on the background as the 1σ uncertainty on the magnitude in the difference image.

If the measured number of electrons/s in the aperture at the position of AT 2018cow is lower than the mean background, or of similar value to the standard deviation of the background, we determine a 3σ upper limit. For this, we measure the number of electrons/s in a circular aperture with 0.08 arcsec radius centred on the position of AT 2018cow and we added three times the standard deviation on the background as described above. The signal-to-noise ratio of the detection of a source in the difference images is determined as the flux density in the source divided by the standard deviation in the flux density in the background.

3 RESULTS

3.1 Astrometry

We find a frame-to-frame alignment uncertainty of 0.005−0.024 arcsec (0.19−0.97 pixels), depending on which combination of frames is looked at. The alignment between images using the same filter is systematically better than alignment between images using different filters.

A relevant question relating to the nature of the late time emission is whether it is dominated by a point-like component that may be due to the transient, or whether it could arise from an underlying compact region. We therefore check if the position of any emission detected in the difference images is consistent with the position of AT 2018cow.

To investigate this we map the early-time UV observations (in particular the F336W data) to the later time F555W observations using 10 compact sources which are likely star forming regions within the host galaxy (see Table B1 for the positions of these sources). We then fit a geometric transformation using GEOMAP, allowing only for a shift in position. The centroid locations for the UV source at 713 d and the compact source in F555W at 1474 d are entirely consistent ($\delta(x) = 0.19 \pm 0.25$ pixels and $\delta(y) = 0.01 \pm 0.19$ pixels). Furthermore, the location of a faint residual visible in the F555W difference image between epoch 1 and epoch 3 is also consistent with the brightest pixel in all epochs of F555W imaging [$\delta(x) = 0.30 \pm 0.36$ pixels and $\delta(y) = 0.06 \pm 0.36$ pixels, where the additional uncertainty arises from the centroid error of the residual emission in the F555W image].

3.2 Photometry

3.2.1 *Aperture photometry*

The results of our aperture photometry can be found in Table 1. In the two UV filters (F225W and F336W) and the F555W filter the source has faded between the first and the third epoch (by 0.55 ± 0.08, 0.39 ± 0.06 and 0.23 ± 0.06 magnitudes, respectively). In the F814W band the magnitudes are consistent with being the same within 3σ.

3.2.2 *Photometry from PSF fitting*

In the right panels of Fig. 1 we show the residuals after PSF subtraction in high contrast for all epochs and filters. The best-fitting position of the centroid of the PSF model (as determined on the F225W $T = 1474$ d image) is marked by red pointers in each image. The left panels show the same images, before subtracting the best-fitting PSF model. In general, the emission in the UV filters subtracts out well while the point source subtraction in the optical filters reveals/highlights the presence of residual emission close to and in some cases under the source position. The magnitudes of the subtracted point sources are listed in Table 1 under PSF photometry. We find reduced χ^2 values between 0.5 and 1.1 for the best fits of the PSF normalization and background value, showing our model describes the data well. Generally, the PSF magnitudes of the subtracted point source are consistent within 3σ with those derived through our aperture photometry for all filters, although the PSF magnitudes in the F814W filter are systematically fainter (but still consistent within 3σ).

Any small residuals present in the PSF-subtracted images obtained through the UV filters can be explained by the fact that the PSF in the UV varies as a function of source location on the image. Due to various factors (such as the coatings of the optical elements) the UV PSF contains broader wings than the optical PSF and these broad wings have complex features.[7] Since we try to fit the central part of the PSF to the data, the features in the wings can leave residuals when a template PSF determined at one place of the image is subtracted from a source at another location in the image.

3.2.3 *Photometry using* DOLPHOT

The results or our PSF photometry using DOLPHOT can be found in Table 1. However, DOLPHOT yields no detection at the position of AT 2018cow in F814W for any of the observation epochs and in F555W at the epoch at $T = 1135$ d, unless the input source position is fixed, as described in section 2.3, which is effectively equivalent to forced photometry at the position of AT 2018cow.

---

[7] https://hst-docs.stsci.edu/wfc3ihb/chapter-6-uvis-imaging-with-wfc3/6-6-uvis-optical-performance

Table 1. The result of our aperture and difference image photometry for AT 2018cow, using a circular aperture of $r = 0.08$ arcsec radius as well as PSF photometry following either our manual procedure (see section 2.3 for details) or using DOLPHOT. 'Diff. image' refers to the image obtained after subtracting the image obtained during the third epoch from the epoch 1 or 2 image under consideration (see section 2.4 for details). Aperture photometry is performed on the diff. images. Values include aperture correction and a Galactic reddening correction as mentioned in the text. To correct for Galactic extinction we have used $A_{\mathrm{F225W}} = 0.524$, $A_{\mathrm{F336W}} = 0.334$, $A_{\mathrm{F555W}} = 0.214$, and $A_{\mathrm{F814W}} = 0.115$. Values without error bars are 3σ upper limits.

Filter	Epoch (d)	# of exp.	Exp. time (s)	Aperture phot. F_ν (μJy)	Aperture phot. (mag)	Diff. image † F_ν (μJy)	Diff. image † (mag)	PSF phot. F_ν (μJy)	PSF phot. (mag)	DOLPHOT F_ν (μJy)	DOLPHOT (mag)
F225W	713	3	1116	1.17 ± 0.06	23.73 ± 0.05	0.45 ± 0.06	24.77 ± 0.14	1.41 ± 0.11	23.53 ± 0.09	1.08 ± 0.06	23.82 ± 0.06
F336W	713	3	1116	0.87 ± 0.04	24.05 ± 0.04	0.28 ± 0.04	25.28 ± 0.15	0.82 ± 0.07	24.11 ± 0.09	0.75 ± 0.03	24.21 ± 0.05
F555W	713	3	1044	0.39 ± 0.02	24.92 ± 0.04	0.09 ± 0.02	26.54 ± 0.25	0.48 ± 0.06	24.69 ± 0.13	0.27 ± 0.06	25.32 ± 0.06
F814W	713	3	1044	0.37 ± 0.03	24.97 ± 0.09	0.11 ± 0.04	$26.3^{+0.4}_{-0.3}$	0.14 ± 0.06	$26.0^{+0.6}_{-0.4}$	0.13 ± 0.2	26.06 ± 0.17
F555W	1135	2	710	0.33 ± 0.02	25.10 ± 0.06	<0.09	>26.5	0.35 ± 0.07	25.07 ± 0.22	0.18 ± 0.02	24.79 ± 0.10
F814W	1135	2	780	0.23 ± 0.03	25.48 ± 0.15	<0.11	>26.3	0.10 ± 0.06	$26.4^{+1.1}_{-0.5}$	0.05 ± 0.02	$27.2^{+0.7}_{-0.4}$
F225W	1474	3	1845	0.71 ± 0.04	24.28 ± 0.06	–	–	0.76 ± 0.08	24.20 ± 0.11	0.54 ± 0.04	24.57 ± 0.07
F336W	1474	3	1953	0.61 ± 0.02	24.44 ± 0.04	–	–	0.54 ± 0.04	24.56 ± 0.08	0.51 ± 0.02	24.63 ± 0.04
F555W	1474	3	1149	0.32 ± 0.01	25.15 ± 0.05	–	–	0.37 ± 0.05	24.98 ± 0.15	0.19 ± 0.01	25.68 ± 0.07
F814W	1474	3	2271	0.29 ± 0.02	25.24 ± 0.07	–	–	0.08 ± 0.04	$26.6^{+0.6}_{-0.4}$	0.08 ± 0.01	26.53 ± 0.17

Note. †This implicitly assumes that any light at the position of the transient at epoch 3 is not due to AT 2018cow.

3.2.4 Aperture photometry on the difference images

Fig. 2 shows the difference images created by subtracting the epoch 3 images from the epoch 1 images for the two optical filters. Here, the position of AT 2018cow is indicated by red markers. In the F555W difference image (left panel) there is residual emission near the position of AT 2018cow. This residual emission is not an artefact due to uncertainties in alignment as there are no such residuals at the positions of other point sources in the difference image. This residual is detected at a signal-to-noise ratio of 4.5 with a magnitude of 26.54 ± 0.25, consistent with the difference between the F555W magnitude in epoch 1 and epoch 3 as measured through aperture photometry.

For the observations obtained in the F814W filter, no distinguishable residual emission is present (when looking by eye) in the difference image, as can be seen in the right panel of Fig. 2. Following the same procedure as for F555W above we find a signal-to-noise ratio of 3.4 with a magnitude of $26.3^{+0.4}_{-0.3}$. Subtracting the epoch 3 image and then measuring the flux/magnitude of the residual measures the decaying component in the AT 2018cow light. An alternative way of looking at the difference image is that it assumes all emission at epoch 3 ($T = 1474$ d) is due to an underlying source at the position of AT 2018cow. Under 'Diff. image' in Table 1, we list our results for aperture photometry on all difference images created by subtracting the epoch 3 from the epoch 1 and epoch 2 images. For the F555W and F814W epoch 2 minus epoch 3 difference images the measured flux density in the aperture is consistent with that expected due to variations in the background, hence we report 3σ upper limits of >26.5 in F555W and >26.3 in F814W.

3.3 Light curve

Out of the three different ways we used to measure the photometry of AT 2018cow the aperture and PSF photometry agree within 3σ. The aperture photometry on the difference images (epoch 1 or epoch 2 minus epoch 3) yield fainter results for the source brightness. This can be explained as follows: through photometry on a difference image we are sensitive only to the component of the light that varied between the epochs under consideration. In the extreme scenario that the third epoch contains *no light* from AT 2018cow the magnitudes determined through analysis of the difference images are relevant. In the opposite extreme scenario, we assume that *all the light* detected at the third epoch comes from AT 2018cow. Clearly, whether either or none of these two is a viable assumption may well depend on the filter of the observations under consideration.

We show the brightness evolution of AT 2018cow as a function of time in Fig. 3, using the results of our aperture photometry on the images and the difference images, together with early time data from Perley et al. (2019) and Sun et al. (2022) (circles). Even though the effective wavelengths of the filters used in the early UVOT and later *HST* observations are slightly different, we compare UVOT/UVW1 to *HST*/F235W, UVOT/U to *HST*/F336W, UVOT/V to *HST*/F555W, and UVOT/I to *HST*/F814W. Different filters are indicated using different colours and we offset the light curve in each filter by a constant shown in the figure legend for display purposes. Our aperture photometry measurements are shown with squares and our measurements for AT 2018cow obtained assuming the third epoch contains no transient emission (aperture photometry on the difference images) are indicated with triangles when a residual was detected or downwards pointing arrows when an upper limit to the source magnitude was determined. Comparing the early-time (<100 d after discovery) measured decay in absolute magnitude with

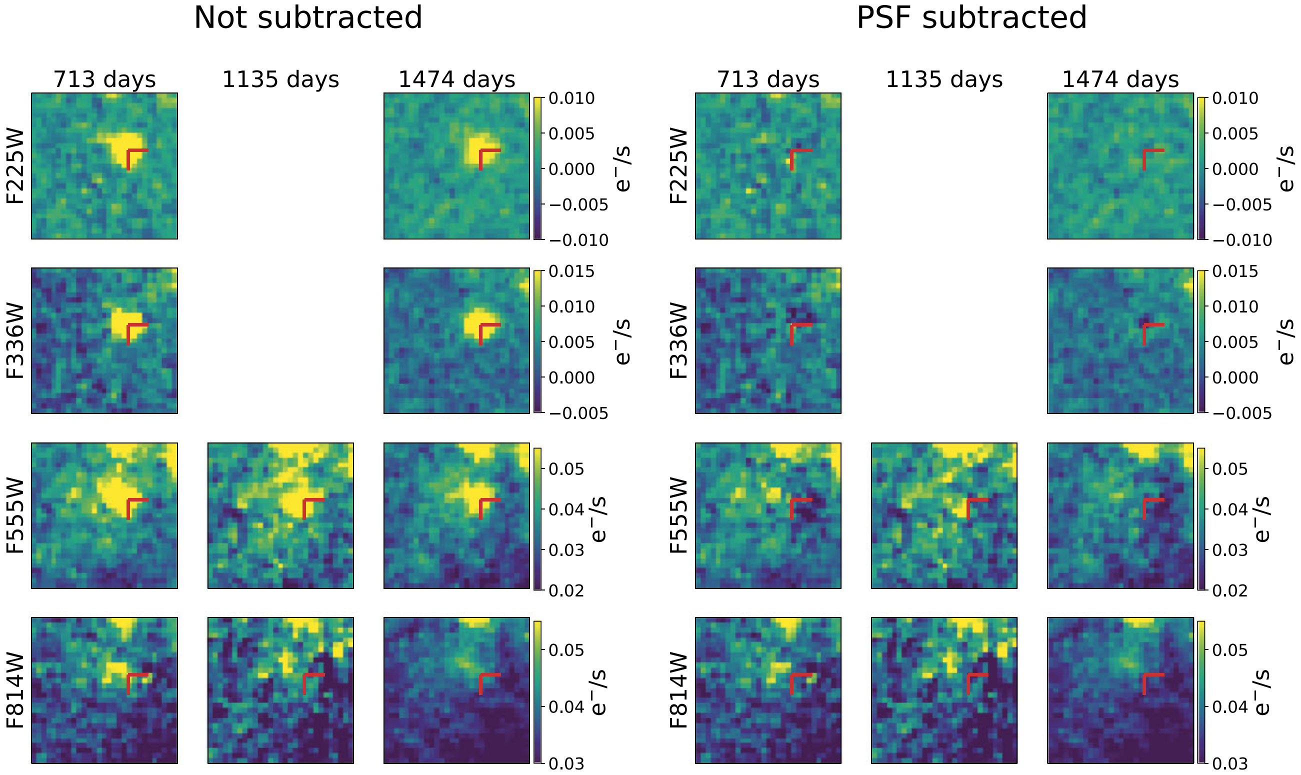

Figure 1. Left panel: Three columns of four rows of cutout images close to the location of AT 2018cow for all filters (rows) and epochs (columns). Intensity is given in e$^-$/s in a colour scale, with blue being the least intense and yellow most intense. The best-fitting centroid position of the PSF to the emission at the location of AT 2018cow lies where the two red lines touch. The cross hairs have a length of 0.1 arcsec. Right panel: Three columns of four rows of cutout images showing the residuals of PSF subtraction at the location of AT 2018cow for all filters (rows) and epochs (columns). The exposure times for the last epoch is longer than for the first two epochs, the second epoch having the shortest exposure time of all, which explains the difference in noise properties in the residual images.

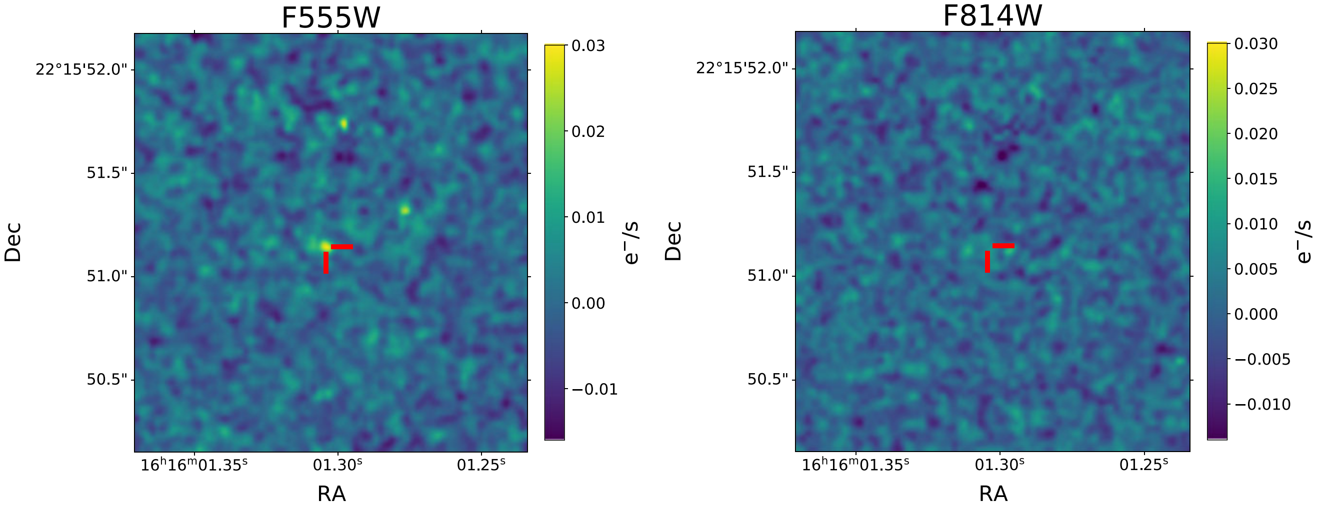

Figure 2. The residual flux after subtracting the image obtained at $T = 1474$ d from the $T = 713$ d image for the two optical filters (F555W left panel; F814W right panel) using HOTPANTS. The location of AT 2018cow is indicated with red thick marks. Residual emission is present at the position of AT 2018cow with a signal-to-noise ratio of 4.5 in the F555W difference image and signal-to-noise ratio of 3.4 in the F814W difference image (left panel; see section 3.2.4 of the main text for details.).

absolute magnitude (limits) obtained for the last three *HST* epochs, it is clear that the detected emission is brighter than expected had this trend continued.

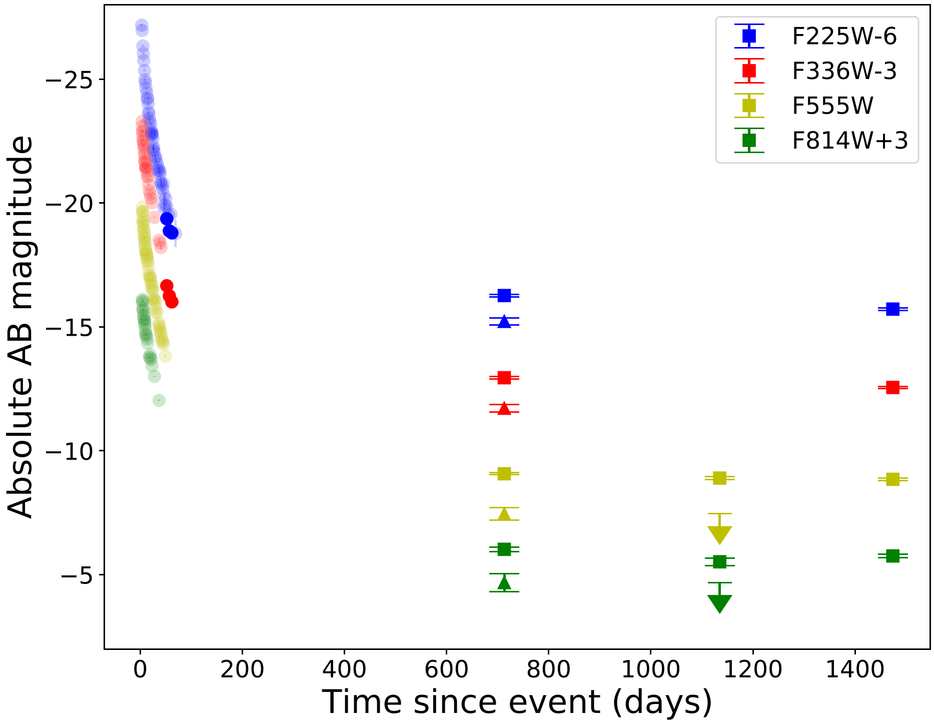

Figure 3. AT 2018cow light curves in different filters, F225W in blue, F336W in red, F555W in yellow, and F814W in green (with offsets as indicated in the legend). The early time data is from Perley et al. (2019) in transparent circles and Sun et al. (2022) in opaque circles. Our aperture photometry results marked with squares assume all flux measured in the last (third) epoch is due to the transient, whereas for the measurements indicated with triangles and downwards pointing arrows (for upper limits) we assumed that all detected flux in epoch three is unrelated to AT 2018cow. The error bars are at a 1σ confidence level. The horizontal bars through the markers do not indicate uncertainties in the observation date but instead they are the end caps of the error bars on the magnitudes.

3.4 Comparison of AT 2018cow and compact UV selected sources

Next, we explore whether AT 2018cow is localized in an unusual region of its host galaxy by fitting synthetic spectra of simple stellar populations to 23 compact UV-selected star-forming (SF) regions within the host (plus the location of AT 2018cow). These SF regions were selected by running SOURCE EXTRACTOR in dual image mode in the same way as for AT 2018cow (see Section 2.2) removing sources that are not detected in all four filters at $T = 713$ d. We also removed sources that are detected with a signal-to-noise ratio <3. From these sources we select those that have a constant magnitude (within 3σ) as measured on $T = 713$ d and $T = 1474$ d. Differences in magnitudes between these epochs might be caused by e.g. different orientations of *HST* during the observations. We ignore epoch 2 in this comparison because the exposure time is shorter and there are only two exposures, resulting in a bad removal of cosmic rays.

Next, we select the sources that behave PSF-like in F336W. We test this by performing aperture photometry using two different values for the radius of the circular aperture and we retained sources only if the difference in their photometry was consistent with the different aperture corrections for a point source given the two different aperture radii. A full list of the positions and magnitudes of the sample can be found in Table C1 in the Appendix C.

To determine the ages of these regions, we make use of BPASS v2.2.1 (Binary Population and Spectral Synthesis; Eldridge et al. 2017; Stanway & Eldridge 2018) synthetic spectra, assuming a single burst of star formation and a metallicity (by mass fraction) of $Z = 0.01$ (based on the host metallicity found by Lyman et al. 2020). For each region, spectral energy distribution (SED) fitting is performed by convolving the BPASS spectra at each age (52 ages spaced logarithmically from 1 Myr to 100 Gyr are used) with the filter response curves for F225W, F336W, F555W, and F814W (Rodrigo, Solano & Bayo 2012; Rodrigo & Solano 2020), converting magnitudes to fluxes, and vertically scaling[8] the synthetic spectra to minimize χ^2 across both age and different values for the host-intrinsic extinction. The extinction in each filter is calculated by adopting their effective wavelengths and using the python EXTINCTION module (Barbary 2016), with a Fitzpatrick (1999) extinction curve and $R_V = 3.1$. Galactic extinction is already accounted for as described in section 2.2.

For each region we determine a best-fitting age and extinction A_V. Full results can be found in Appendix C. The extinction values are in the range 0.0–0.6 (in broad agreement with $A_V = 0.2$ as found by Sun et al. 2023, for nearby star forming complexes), and the ages range from 6 to 25 Myr. These ages are younger than the tens of Myr found by Lyman et al. (2020) for example, but this can be explained by the spaxel size of their MUSE integral field unit data, which averages over larger physical areas than the compact SF regions we are probing here.

The reduced χ^2 values (which are the same as the χ^2 values because our fit has one degree of freedom) for the 23 compact SF regions are typically around ∼1–10; whereas the fits at the location of AT 2018cow (at both 713 and 1474 d) are notably poorer, with $\chi^2 = 47$ and 37, respectively. The fits at the location of AT 2018cow favour very little to no extinction, and tellingly, favour the youngest

---

[8] The scaling is needed as the synthetic spectra are for a 10^6 $M_\odot$ population, in Solar luminosity per Angstrom

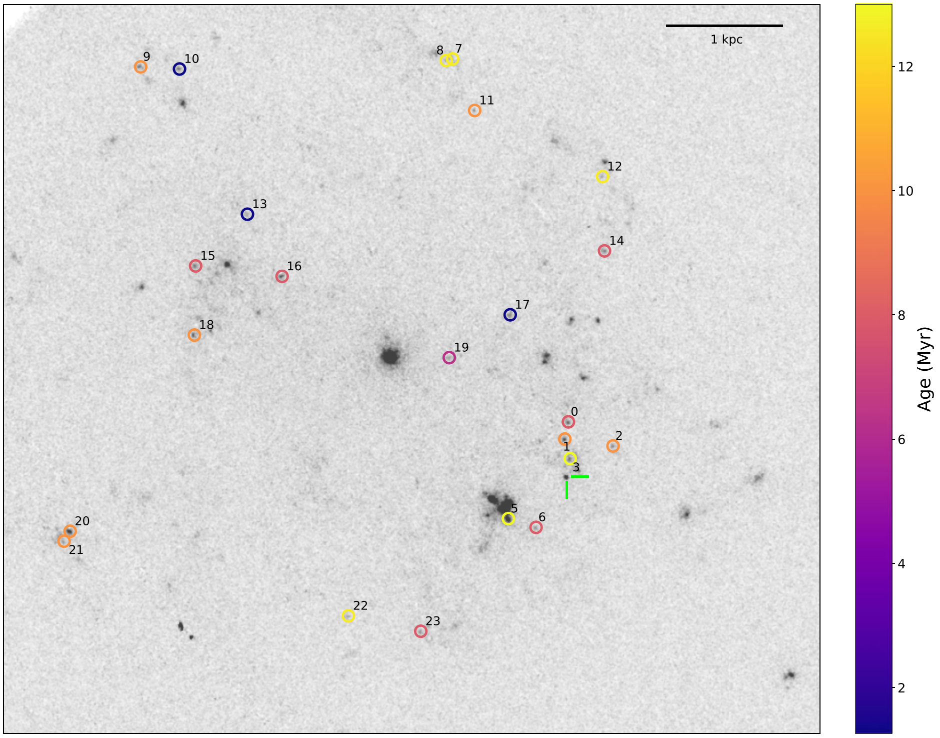

Figure 4. Grey scale image of the host galaxy of AT 2018cow in the F336W filter at $T = 713$ d, with the ages of compact UV-selected sources that were detected in all four filters indicated by coloured circles. The colours correspond to population ages, indicated by the colour bar and derived from BPASS SED fitting as described in Section 3.4. The location of AT 2018cow is marked by green cross hairs. Number labels for the regions are as in Table C1.

population age available in the BPASS outputs (1 Myr), whilst still failing to reproduce the extremely blue observed SED.

In Fig. 4, we show the 23 UV-selected SF regions over an F555W image of the host galaxy. Each of the 23 regions is encircled, where the colour of the circle corresponds to the best-fitting population age. Young stellar populations are present across the galaxy, with no preference for particularly young SF regions in the vicinity of AT 2018cow, although there are two SF regions within ∼400 parsec of the transient (regions 1 and 3, these were unresolved in previous non-*HST* data sets).

3.5 Spectral energy distribution of AT 2018cow

Fig. 5 (left panel) shows the SEDs for AT 2018cow as measured at epoch 1 ($T = 713$ d) and at epoch 3 ($T = 1474$ d). The black markers represent measurements from the third epoch, while the grey markers those of the first epoch. The marker symbols are the same as in Fig. 3. The coloured bands represent the FWHM of the filter with the corresponding colour in Fig. 3.[9] The right panel of Fig. 5 shows both possible extremes of the SED of AT 2018cow in red compared to the SEDs of compact UV-selected sources detected in a box of 180 × 180 pixels centred on the position of AT 2018cow (neighbours) in green, and ‘other sources’ in the rest of the host galaxy in grey for $T =$ 713 d. From this red shaded region it is clear that for either of the two extreme scenarios for the aperture photometry at epoch $T = 713$ d, the F555W−F225W colour of AT 2018cow is bluer than that of the neighbours. The left panel of Fig. 5 shows that the SED for the third epoch lies in between the aperture photometry SED and the difference image SED. Therefore, the $T = 1474$ d SED is also bluer than that of the neighbours.

We fit a Planck function to the four-filter SEDs at $T = 713$ d, $T = 1474$ d, and to the four-filter SED when assuming none of the third epoch emission is due to AT 2018cow, with the best-fitting blackbody overplotted in the left panel of Fig. 5 in orange, green, and blue, respectively. The best-fitting values for the temperature and radius, the calculated luminosity, the number of degrees of freedom, and the reduced χ^2 values are presented in Table 2. The error on the temperature for the fit to the epoch 1–epoch 3 difference image was calculated by fixing the radius to the best-fitting value and finding the value for which $\Delta\chi^2 = 1$. This was done because the error calculated by the fitting algorithm was larger than the best-fitting value for the temperature. Only the reduced χ^2 value for the fit to the epoch 1 SED derived assuming epoch 3 contains no light from AT 2018cow is close to 1 (at a value of 2.2). However, the error on the luminosity is very large due to the large errors on the radius. Due to the sizes of the error bars on the magnitudes obtained with aperture photometry on the difference image, the fit of the Planck function is dominated by the two data points in the UV bands, meaning the fit is almost degenerate for a two-parameter Planck function. This results in a large error on the fit and therefore on the calculated luminosity.

4 DISCUSSION

In this paper, we present aperture and PSF photometry of *HST* data of the FBOT AT2018cow. We first compare our results in Table 1 with the results from the epoch 1–3 PSF photometry by Sun et al. (2022, 2023). We find that our measurements in the UV filters yield a source that is consistent within 3σ in the first epoch, while in the last epoch

---

[9] https://hst-docs.stsci.edu/wfc3ihb/chapter-6-uvis-imaging-with-wfc3/6-5-uvis-spectral-elements

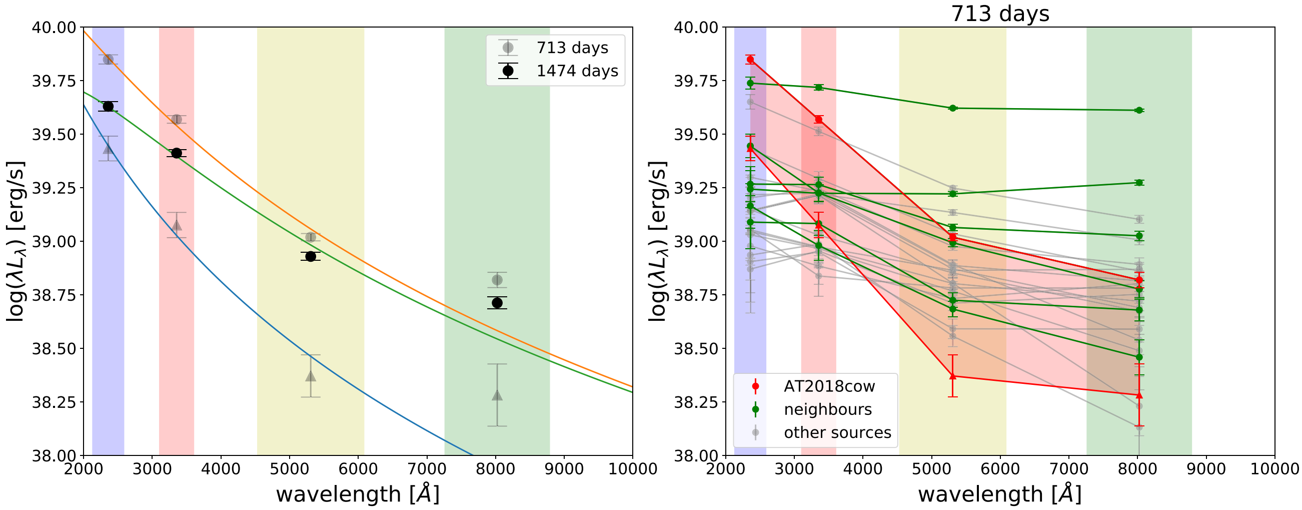

Figure 5. Left panel: The SED of the emission detected at the position of AT 2018cowat $T = 713$ d and $T = 1474$ d. The four vertical coloured bands are centred on the effective wavelength of the filters used for the observations while the width of the vertical bands indicate the passband rectangular width of the filters. Light grey markers are used for the data obtained at $T = 713$ d. Here, the light grey circles indicate the measured flux density assuming all light in the third epoch ($T = 1474$ d) originates from AT 2018cow, whereas light grey triangles are used for measurements obtained assuming none of the third epoch light is due to AT 2018cow. The circles are always at a higher flux density than the triangles. The black symbols represent our measurements of the source flux density obtained at $T = 1474$ d. The lines are Planck functions fitted to the four-point SEDs at $T = 713$ d (orange), $T = 1474$ d (green), and to the grey triangles (blue). The best-fitting values for the temperature and the radius, and reduced χ^2 values can be found in Table 2. The fit to the difference image gave unphysical (a negative) values for the temperature when considering the uncertainty on the temperature using both python routines CURVE_FIT and LMFIT. To obtain an estimate of the uncertainty on the blackbody temperature we fixed the radius to the best-fitting value and determine for which value for the temperature around the best-fitting temperature value $\Delta\chi^2 = 1$. From the reduced χ^2 values and the figure we conclude that a single blackbody function is only a reasonably good description of the SED for the light grey triangles. Right panel: The SEDs of our list of compact UV-detected sources at $T = 713$ d (Table C1 contains selected properties of these sources). The data for AT 2018cowis in red with the marker shapes as mentioned above. We make a distinction between 'neighbours' shown in green and 'other sources' in light grey. See the main text for the definition of 'neighbour' and 'other sources'. Irrespective of the interpretation of the AT 2018cow data at $T = 1474$ d, the F555W−F225W colour of the source at the position of AT 2018cow is bluer than any of our compact UV-detected sources.

Table 2. Results from fitting a Planck black body function to the *HST* SED for AT 2018cow. These fits are shown in Fig. 5.

Epoch	log (T (K))	Radius ($R_\odot$)	Luminosity (erg s^{-1})	Reduced χ^2	Degrees of freedom
1: $T = 713$ d	4.54 ± 0.04	34 ± 3	$(6 \pm 2) \times 10^{39}$	17.2	2
3: $T = 1474$ d	4.37 ± 0.02	43 ± 2	$(1.9 \pm 0.4) \times 10^{39}$	17.9	2
Epoch 1–Epoch 3	5.03 ± 0.04	9 ± 6	$(4^{+5}_{-4}) \times 10^{40\dagger}$	2.2	2

Note. † See Section 3.5 for the explanation on how the error bars on the luminosity were determined.

our source is brighter than they report (there are no UV images for the second epoch). In the optical filters our measurements indicate a brighter source in all epochs than found by Sun et al. (2022, 2023). They assumed all the light is emitted by AT 2018cow. Additionally, Sun et al. (2022, 2023) find a steeper decay between epoch 1 and 3 in the UV filters (1.02 ± 0.11 mag and 0.57 ± 0.07 mag for F225W and F336W, respectively) than we do (0.55 ± 0.08 mag and 0.39 ± 0.06 for F225W and F336W, respectively). Furthermore, they find no evidence for a decay in the source brightness in the optical filters, whereas we do (0.23 ± 0.06 mag in F555W, and a detection with a signal-to-noise ratio of 3.4 in the F814W epoch 1 and epoch 3 difference image with a magnitude of $26.3^{+0.4}_{-0.3}$). We will investigate possible reasons for these differences below.

Next, we compare with the epoch 1–3 PSF photometry reported in Chen et al. (2023). Our aperture as well as our manual PSF photometry give brighter magnitudes for AT 2018cow than Chen et al. (2023), although the difference is small for the two UV filters it increases for the optical filters. Comparing the magnitudes in the Chen et al. (2023) table 1 with their fig. 6 we deduced that their table 1 magnitudes are corrected for extinction. However, if they are not, the differences with our extinction-corrected magnitudes is reduced, especially for the UV filters. However, still, only the measurements in F225W (both epochs) and F555W $T = 1135$ d would be consistent within the 3σ error. Our DOLPHOT PSF photometry results are consistent within 3σ with the values presented by Chen et al. (2023) in their table 1 if those values are not corrected for Galactic extinction. When leaving the position as a free parameter, DOLPHOT does not find a source in F814W at any epoch and also not in F555W at the epoch $T = 1135$ d. Only forced photometry (i.e. keeping the source position fixed) yields a sometimes marginal detection of the source at those epochs and filters.

However, this does not necessarily mean the photometry presented by Sun et al. (2022, 2023), Chen et al. (2023), or our photometry results are wrong. In practice, contributions from other sources besides a point source may influence the measurements, or if no point source is present but if the observed light is dominated by diffuse emission (on the scale of ∼few times the PSF size) in AT 2018cow's host galaxy galactic disc, PSF photometry provides

Table 3. The result of our aperture photometry for AT2018cow, using a circular aperture of $r = 0.08$ arcsec radius for three different values of the background (see the main text for details). The reported magnitudes include the effect of the aperture correction and the Galactic reddening correction. To correct for Galactic extinction we used $A_{\mathrm{F225W}} = 0.524$, $A_{\mathrm{F336W}} = 0.334$, $A_{\mathrm{F555W}} = 0.214$, and $A_{\mathrm{F814W}} = 0.115$. The errors reported are at the 1σ confidence level.

Filter	Epoch	Min background F_ν (μJy)	Min background (mag)	Median background F_ν (μJy)	Median background (mag)	Max background F_ν (μJy)	Max background (mag)
F225W	713	1.28 ± 0.06	23.63 ± 0.05	1.18 ± 0.06	23.71 ± 0.05	1.07 ± 0.06	23.82 ± 0.06
F336W	713	0.95 ± 0.04	23.95 ± 0.05	0.88 ± 0.04	24.02 ± 0.05	0.78 ± 0.04	24.16 ± 0.06
F555W	713	0.49 ± 0.05	24.68 ± 0.11	0.40 ± 0.05	24.92 ± 0.14	0.30 ± 0.05	25.22 ± 0.19
F814W	713	0.57 ± 0.12	24.50 ± 0.22	0.41 ± 0.12	24.9 ± 0.3	0.18 ± 0.12	$25.8^{+1.2}_{-0.6}$
F555W	1135	0.42 ± 0.05	24.85 ± 0.13	0.33 ± 0.05	25.10 ± 0.17	0.25 ± 0.05	25.41 ± 0.22
F814W	1135	0.46 ± 0.12	24.8 ± 0.4	0.26 ± 0.12	$25.4^{+0.7}_{-0.4}$	$<0.34^{\dagger}$	$>25.1^{\dagger}$
F225W	1474	0.76 ± 0.03	24.19 ± 0.05	0.70 ± 0.03	24.28 ± 0.05	0.65 ± 0.3	24.37 ± 0.05
F336W	1474	0.65 ± 0.03	24.37 ± 0.05	0.61 ± 0.03	24.43 ± 0.05	0.51 ± 0.03	24.64 ± 0.07
F555W	1474	0.40 ± 0.05	24.88 ± 0.14	0.32 ± 0.05	25.13 ± 0.17	0.22 ± 0.05	25.53 ± 0.25
F814W	1474	0.47 ± 0.13	24.7 ± 0.3	0.30 ± 0.13	$25.2^{+0.6}_{-0.4}$	$<0.43^{\dagger}$	$>24.8^{\dagger}$

Note. †The flux density value of the background was higher than that in the aperture centred on the position of AT 2018cow, so we report the 3σ upper limit for the maximum background flux density.

an upper limit on the magnitude of a point source at the location of AT 2018cow. Instead, aperture photometry may overestimate the true flux density of the transient if the light from the point source and diffuse emission in the galactic disc are of similar magnitude. In practice, the estimated value of the background flux density under AT 2018cow may influence the determined magnitudes especially in crowded regions like that of AT 2018cow. Next, we investigate the potential influence of the choice of the background region used to estimate the flux density at the position of AT 2018cow.

Using the same 20 background regions we used for the aperture photometry on the difference images (see Fig. A1), we measure the median, minimum, and maximum value for the flux density in the background aperture. There is a large spread between these three values. To investigate how the choice of background region influences the flux density measured for AT 2018cow, we compare the results based on which of these three values is subtracted from the flux density measured in the aperture centred on the position of AT 2018cow. In Table 3 we show the resulting magnitude measurements for the different background regions. As expected, we find that using a higher background flux density yields a lower flux density for AT 2018cow. Depending on the choice of background in our work and in the work of Chen et al. (2023) both results could be consistent in all filters. We do note that in the F814W filter when using the maximum background flux density, our results are either upper limits when the maximum background flux density was higher than the flux density in the aperture of AT 2018cow, or there are large error bars on our photometry. Clearly, the region used to determine the background flux density greatly influences the value of the magnitude of AT 2018cow.

Next, we investigate if there are filters and epochs where the detected light originates solely from AT2018cow, or if it is possible to determine if the emission is dominated by underlying sources (for instance from diffuse emission in the galactic disc or e.g. an SF region or cluster) or if it is a combination of both. Understanding the origin of the light is important because it will influence the interpretation of the power source of AT 2018cow.

In the observations obtained through the UV filters the magnitude has decreased between epochs, suggesting that a significant fraction of the detected light is emitted by the fading transient. The SED of the light extracted at the position of AT 2018cow is substantially bluer than that of our compact, UV-selected, SF regions detected throughout the host of AT2018cow. This is also in line with the notion that the majority, but not necessarily all, of the light detected in the UV arises from the transient. Subtracting a point source from the UV images at the location of AT 2018cow, leaves residuals consistent with noise (see Fig. 1). Therefore, we conclude that the emission in the UV filters is dominated by a point source, likely the transient event AT 2018cow. In the optical filter images, comparing the observations at epoch 1 with those at epoch 3 there is evidence that the source faded in addition to light from either AT 2018cow (constant) and/or underlying emission from part of the host galaxy itself.

Overall, a picture emerges where light from the transient is still detected in the UV images, while in optical images we cannot determine if the detected light at epoch 3 is due to AT 2018cow or due to diffuse emission in the galactic disc or, more speculatively, due to a compact source at the same position of AT 2018cow. Note that in the optical images crowding is more important than in the UV images.

The SED of the emission detected at the location of AT 2018cow is consistent with this picture (Fig. 5). While the F814W-F555W colour of AT 2018cow is consistent with that of the neighbouring sources, the F336W-F225W colour at the location of AT 2018cow is bluer than that of the sources in the neighbourhood. This and the fact that a single blackbody does not fit the SED, together with the different variability properties of the UV and optical filters, suggests that the UV and optical parts of the SED are caused by more than one emission type and/or by more than one source. This conclusion does not depend on the assumption for the nature of the light detected at 1474 d (either transient or environment light or a combination thereof). Furthermore, the emission cannot be solely from a stellar population – it is too blue – strongly implying the presence of late-time UV emission from AT 2018cow.

We also searched for BPASS single and binary stellar models, across all possible stellar ages (at $Z = 0.010$), for models satisfying $\log_{10}(\mathrm{T/K}) > 4.7$ and $\log_{10}(\mathrm{L/L_{\odot}}) > 7.0$. These constraints are derived from fitting a blackbody to the late-time emission at the location of AT 2018cow (see also Sun et al. 2023). We find no stellar models which are this blue and luminous, and therefore, a dominant contribution from an underlying massive star or binary seems ruled out by the data.

The F555W-F814W colour at the location of AT 2018cow at 1474 d is $= -0.09 \pm 0.08$ and the absolute magnitude is ~ -9.

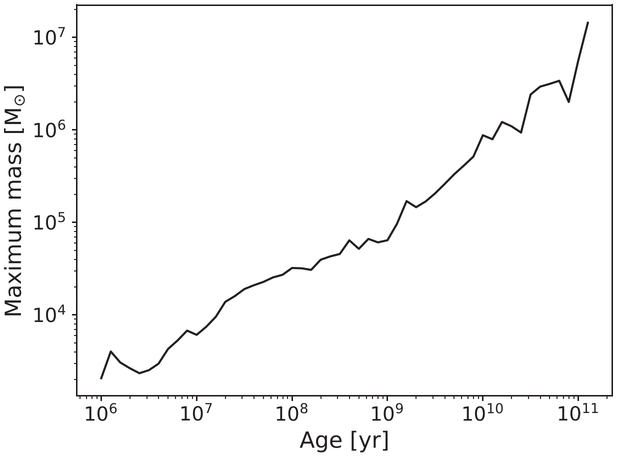

Figure 6. The maximum mass of a stellar cluster that can be underlying AT 2018cow as a function of population age. This is determined by the maximum luminosity of a BPASS simple stellar population that can lie at this location without the luminosity in one of the four *HST* bands exceeding the observed value.

Assuming that the optical bands at epoch 3 are free from light originating from the transient (as we do when taking the magnitudes measured on the difference images), we check what kind of source(s) can explain these values. They are consistent with those expected for an OB association or SF region (e.g. Drazinos et al. 2013), and they are broadly consistent with the F555W-F814W colours of the UV-selected, compact star-forming regions shown in Fig. 4. The mean F555W-F814W colour [corrected for Galactic but not intrinsic extinction (at the specific location in the host galaxy)] of these regions is 0.02 ± 0.05. Excluding the UV filters, fixing $A_{\rm V} = 0$ and performing SED fitting as described in section 3.4, we infer a best-fitting population age at the location of AT 2018cow of 20 and 79 Myr at 713 and 1474 d, respectively. Although we cannot determine a precise age with just two optical filters, if we assume no extinction and that the optical light is dominated by the underlying stellar population, the optical spectral slope constrains the age to ∼100 Myr or less.

Taking the 4-band photometry of AT 2018cow (latest epoch with the median background, see Table 3), and converting it to absolute magnitudes and using BPASS simple stellar populations, we calculate the maximum mass of a cluster that can be present at the location of AT 2018cow before the luminosity in one of the filters exceeds the magnitude plus its $1\,\sigma$ error. We plot the upper limit on the cluster mass in Fig. 6. This upper limit is a strong function of age – as the UV flux reduces with increasing age, the upper limit on the cluster mass increases. An old stellar population at the location of AT 2018cow cannot be ruled out – in particular, we note that a globular cluster can easily be hidden underneath the light of AT 2018cow (based on typical globular cluster ages of several Gyr and masses of 10^3–10^6M$_\odot$; Harris 1996).

4.1 Disc modelling

It has been speculated that AT 2018cow is caused by a TDE (e.g. Kuin et al. 2019; Perley et al. 2019). Interestingly, for low mass ($M_{\rm BH} < 10^{6.5} M_\odot$) TDEs roughly time-independent UV emission lasting for time-scales of years is commonly detected (van Velzen et al. 2019; Mummery & Balbus 2020; Wen et al. 2023). Comparing the UV light curve of AT 2018cow (Fig. 3) with that of TDEs, for example ASSASN-14li (see e.g. fig. 2 in Wen et al. 2023), we note that the UV light-curve morphology is similar. Especially the late-time plateau is a distinguishing feature shared by both sources.

To test the hypothesis if the late-time UV emission observed from AT2018cow could come from an evolving accretion flow produced by the tidal disruption of a star by a massive black hole, we follow the procedure set out in Mummery & Balbus (2020), and generate evolving UV light curves by solving the time-dependent general relativistic thin disc equations. In brief, we assume that the tidal disruption of a star results in the formation of a compact ring of material with total mass roughly half that of the disrupted star. This initial ring is assumed to form at the circularization radius (typically twice the tidal radius) of the incoming star (see also Hayasaki & Jonker 2021). Once this initial condition is specified, by solving the time-dependent relativistic disc equations, the disc density can be propagated out to large times. Once the dynamical evolution of the disc density is solved, the observed disc spectrum can be computed by ray-tracing the emergent flux of each disc annulus. This then allows us to compute late time UV luminosities for a range of black hole and stellar parameters.

The late-time luminosity observed from the location of AT2018cow is, compared to the typical TDE population, at a relatively low level $\nu L_\nu \simeq 10^{39}$ erg s^{-1}, at $\nu \simeq 10^{15}$ Hz. This is much smaller than, for example, the luminosity of the $\sim 10^6 M_\odot$ black hole mass TDE ASASSN-14li, which had a late time (>1 yr) UV luminosity of $\nu L_\nu \simeq 10^{42}$ erg s^{-1}. Mummery (2021) showed empirically from fitting the light curves of nine TDEs that the late time UV plateau luminosity correlates approximately linearly with the black hole mass responsible for the TDE. This empirical result has strong theoretical and numerical support (Mummery et al. 2023), and suggests that AT2018cow could well be due to a TDE involving an intermediate-mass central black hole.

To test this hypothesis, we numerically sample $N = 10^5$ black hole masses uniformly in the range $10^1 < M_{\rm BH}/M_\odot < 10^7$. At each black hole mass we sample stellar masses from the Kroupa IMF (Kroupa 2001), solve the disc equations, and 'observe' the system at a random inclination [with $\cos(i)$ sampled uniformly]. We sample uniformly the (dimension-less) black hole spin between $-1 < a < 1$. As a very conservative constraint on the central black hole mass in AT2018cow, we record all TDE disc systems which produce a UV luminosity at + 713 d (the time of the first *HST* observation) within a factor of 2 of 3×10^{39} erg s^{-1} at $\nu = 10^{15}$ Hz. The black hole mass distribution of the TDE systems which satisfy this constraint are shown in Fig. 7.

A more detailed analysis of the late time AT2018cow light curve and spectrum highlights that an evolving accretion flow provides a plausible explanation of the observed AT2018cow data. It is of course difficult to constrain a best-fitting set of parameters from observations in two bands at two epochs, and we do not attempt to measure the precise system parameters of AT2018cow from the late time *HST* data. Instead, we examine a subset (200) of our solutions (Fig. 7) which produce particularly 'good fits' (as judged by their chi-squared statistic computed from both epochs). For these solutions we generate both optical-UV spectra at $t = +713$ d and +1474 d, and disc UV light curves from $t = 0$ to $t = +1500$ d. These disc spectra and light curves are displayed in Figs 8 and 9, respectively. It is clear that an evolving relativistic accretion flow can reproduce the observed late-time properties of AT2018cow.

The central black hole masses inferred from disc modelling ($M_{\rm BH} \sim 10^{3.2\,\pm\,0.8} M_\odot$) implies that the early-time UV/optical emission observed from AT2018cow is significantly above the Eddington luminosity $L_{\rm Edd} \simeq 10^{41}(M_{\rm BH}/10^3 M_\odot)$ erg s^{-1}. If the early time luminosity is indeed ultimately powered by accretion (which is still uncertain, see e.g. Roth et al. 2020), then it is unlikely that the thin

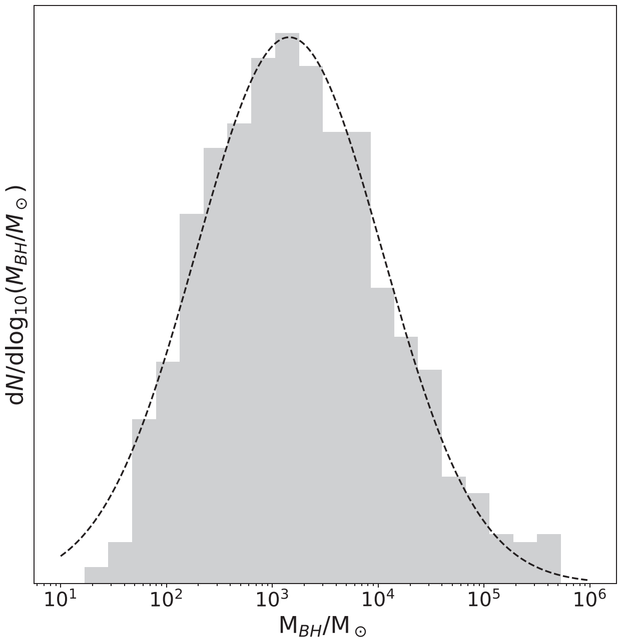

Figure 7. The black hole masses consistent with the assumption that AT 2018cow was caused by a TDE. The distribution of black hole masses has been derived assuming the late time UV emission is due to the accretion disc formed following the disruption (see the main text for details). The mean of the logarithm of black hole mass ($M_{\rm BH}$) is $\log\ M_{\rm BH} = 3.2 \pm 0.8$ (with the mass in $M_\odot$).

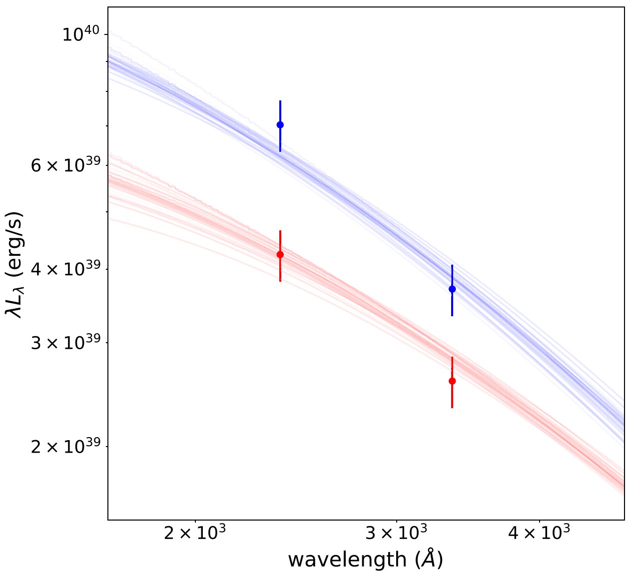

Figure 8. Late time (blue = +713 d, red = + 1474 d) spectral snapshots of a sample of relativistic accretion disc models for AT 2018cow. These curves show a subset of the disc models (Fig. 7) which produced particularly good fits to the data.

disc models used here would be valid at these very early times (i.e. for the first ∼ 100 d). However, by the much later times, which we are interested in, the bolometric luminosities of the disc solutions are typically at the level of a few 10^{40} erg s^{-1} (e.g. Fig. 8), suggesting Eddington ratios at the 10 per cent level, where thin disc models are valid.

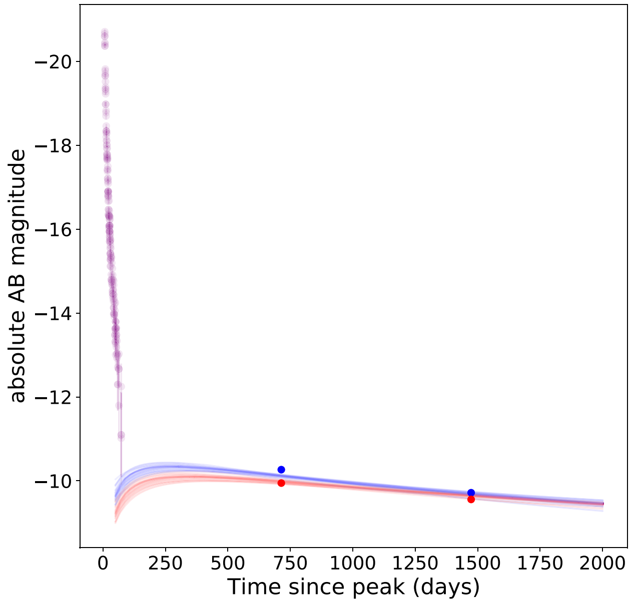

Figure 9. The light curves of the relativistic disc models which produce the spectra displayed in Fig. 8. The late time *HST* data are displayed in blue (F225W) and red (F336W). Early time data in the ultraviolet bands UVW1, UVW2, and UVM2 are displayed in purple. Importantly, a disc model can reproduce the late time AT 2018cow UV emission, without modifying the observed early time AT 2018cow rapid light-curve decline. There is no consensus in the TDE community about the origin of the early-time UV (and optical) emission (see e.g. Roth et al. 2020). The error bars are at a 1σ confidence level, and may be smaller than the marker size.

Chen et al. (2023) uses a steady state disc model to fit their T = 1474 d SED and obtain an estimate for the mass for the BH. However, steady state disc theory predicts an optical/UV disc luminosity which scales as $(M_{\rm BH}\dot{M})^{2/3}$. This optical/UV luminosity is thus highly degenerate between the (unknown) mass accretion rate $\dot{M}$, and the black hole mass $M_{\rm BH}$ (e.g. Frank, King & Raine 2002). However, the late time disc temperature profile in a TDE disc is constrained, as the total initial mass, radial, and temporal scales of the disc are known a priori for a given stellar disruption. This initial mass content must then propagate radially according to the standard laws of mass and angular momentum conservation. The resulting late-time optical/UV luminosity of a *TDE disc* is strongly constrained. We make use of this in our disc model.

If AT 2018cow is indeed a TDE, the short time-scale and the disc modelling suggests a relatively low-mass BH was responsible for the disruption. Pasham et al. (2021) find a limit of $M_{\rm BH} < 850 M_\odot$ based on the frequency of the soft QPO. Zhang et al. (2022) find a low frequency QPO, corresponding to a BH mass of $\sim 10^4 M_\odot$ and they suggest the maximum mass found by Pasham et al. (2021) can be increased to higher mass adding a binary component to the compact object.

A problem for the TDE hypothesis is that the BH responsible for the disruption needs to be embedded in a dense stellar environment for dynamical friction to be efficient enough to bring a star on an orbit towards its tidal radius within a Hubble time (e.g. Stone & Metzger 2016). Such a dense stellar environment where dynamical interactions occur often enough, may arise in nuclear star clusters, dense young star clusters, or globular clusters. There is evidence of a recent interaction between CGCG 137-068 and a companion galaxy from a ring of high column density gas as well as from a faint tidal tail (Roychowdhury, Arabsalmani & Kanekar 2019; Lyman et al. 2020). If the host galaxy underwent a recent (minor) merger it is conceivable that an IMBH or SMBH, with its nuclear star cluster, is in the process of falling into the centre of CGCG 137-068. This means that a TDE origin of AT 2018cow remains a viable possibility.

However, Michałowski et al. (2019) attributes the presence of the ring of high column density gas reported by Roychowdhury et al. (2019) to internal processes instead of a galaxy merger/interaction. Their observations using H I show no evidence for a concentration of gas near the location of AT 2018cow. They conclude that the host of AT 2018cow differs from the hosts of GRBs/SNs in its properties and therefore the environment of AT 2018cow does not provide evidence for a massive star progenitor for the event, leaving the question on the nature of AT 2018cow wide open.

5 SUMMARY AND CONCLUSIONS

Using three epochs of *HST* observations we investigate the late-time UV and optical emission at the location of AT 2018cow. The main results are that AT 2018cow remains UV-bright, even with evidence for fading in the UV filters (F225W and F336W) between the first and third epoch of *HST* observations. The magnitude of AT 2018cow in the optical filters (F555W and F814W) can differ by up to a magnitude depending on how the (diffuse galaxy) background at the location of AT 2018cow is determined.

From our analysis we conclude the following: (i) The observed UV emission is consistent with being dominated by a fading point source which originates most likely from AT 2018cow. (ii) While part of the optical emission could be due to slowly decaying emission from the transient, there is evidence for a contribution of underlying emission, that did not fade between epochs. Some fraction of this could originate in diffuse galactic background light or an underlying point(like) source. (iii) The late-time UV emission is reminiscent of late-time UV emission seen for TDEs. The late-time UV luminosity of AT 2018cow is consistent with the disruption of a (low-mass) star by an IMBH. For this scenario to be feasible AT 2018cow needs to reside in a dense (young/old) stellar cluster.

Our research shows that the nature of AT 2018cow is still uncertain. Both model scenarios involving either specific massive star evolution or a tidal disruption of a (WD) star by an IMBH have their advantages and disadvantages.

ACKNOWLEDGEMENTS

AI thanks Luc IJspeert for helpful discussions. This work is part of the research programme Athena with project number 184.034.002, which is financed by the Dutch Research Council (NWO). The scientific results reported on in this article are based on data obtained under *HST* Proposals 15974, 16179, and 16925 with PI A.J. Levan, A. Filippenko, and Y. Chen, respectively. This work was supported by a Leverhulme Trust International Professorship grant [number LIP-202-014]. This work makes use of Python packages NUMPY (Harris et al. 2020), SCIPY (Virtanen et al. 2020); MATPLOTLIB (Hunter 2007), EXTINCTION (Barbary 2016), and DRIZZLEPAC (Hoffmann et al. 2021). This work made use of ASTROPY:[10] a community-developed core Python package and an ecosystem of tools and resources for astronomy (Astropy Collaboration 2013, 2018, 2022). This research made use of PHOTUTILS, an Astropy package for detection and photometry of astronomical sources (Bradley et al. 2022). This research has made use of the SVO Filter Profile Service (http://svo2.cab.inta-csic.es/theory/fps/) supported from the Spanish MINECO through grant AYA2017-84089 (Rodrigo et al. 2012; Rodrigo & Solano 2020). This work has made use of v2.2.1 of the Binary Population and Spectral Synthesis (BPASS) models as described in Eldridge et al. (2017) and Stanway & Eldridge (2018).

DATA AVAILABILITY

All data used in this paper is publicly available from the Mikulski Archive for Space Telescopes. A reproduction package for this paper is uploaded to Zenodo (https://doi.org/10.5281/zenodo.8246571).

REFERENCES

Adelman-McCarthy J. K. et al., 2008, ApJS, 175, 297
Arcavi I. et al., 2016, ApJ, 819, 35
Arnett W. D., 1982, ApJ, 253, 785
Astropy Collaboration 2013, A&A, 558, A33
Astropy Collaboration 2018, AJ, 156, 123
Astropy Collaboration 2022, ApJ, 935, 167
Barbary K., 2016, extinction v0.3.0. Available at: https://doi.org/10.5281/zenodo.804967
Becker A., 2015, HOTPANTS: High Order Transform of PSF ANd Template Subtraction, Astrophysics Source Code Library, record ascl:1504.004
Bellm E. C. et al., 2019, PASP, 131, 018002
Bertin E., Arnouts S., 1996, A&AS, 117, 393
Bradley L. et al., 2022, astropy/photutils: 1.5.0. Available at: https://doi.org/10.5281/zenodo.6825092
Burrows D. N. et al., 2005, Space Sci. Rev., 120, 165
CHIME Collaboration 2022, ApJS, 261, 29
Chen Y., Drout M. R., Piro A. L., Kilpatrick C. D., Foley R. J., Rojas-Bravo C., Magee M. R., 2023, preprint (arXiv:2303.03501)
Coppejans D. L. et al., 2020, ApJ, 895, L23
Dolphin A. E., 2000, PASP, 112, 1383
Drazinos P., Kontizas E., Karampelas A., Kontizas M., Dapergolas A., 2013, A&A, 553, A87
Drout M. R. et al., 2014, ApJ, 794, 23
Eldridge J. J., Stanway E. R., Xiao L., McClelland L. A. S., Taylor G., Ng M., Greis S. M. L., Bray J. C., 2017, Publ. Astron. Soc. Austr., 34, e058
Fitzpatrick E. L., 1999, PASP, 111, 63
Fox O. D., Smith N., 2019, MNRAS, 488, 3772
Frank J., King A., Raine D. J., 2002, Accretion Power in Astrophysics: Third Edition. Cambridge Univ. Press, Cambridge, UK
Harris W. E., 1996, AJ, 112, 1487
Harris C. R. et al., 2020, Nature, 585, 357
Hayasaki K., Jonker P. G., 2021, ApJ, 921, 20
Ho A. Y. Q. et al., 2020, ApJ, 895, 49
Ho A. Y. Q. et al., 2023, ApJ, 949, 120
Hoffmann S. L., Mack J. et al., 2021, 'The DrizzlePac Handbook', Version 2.0. STScI, Baltimore
Hunter J. D., 2007, Comput. Sci. Eng., 9, 90
Jonas J., MeerKAT Team, 2016, in PoS: MeerKAT Science: On the Pathway to the SKA. Sissa Medialab, Stellenbosch, South Africa, p. 1
Kroupa P., 2001, MNRAS, 322, 231
Kuin N. P. M. et al., 2019, MNRAS, 487, 2505
Lacy M. et al., 2020, PASP, 132, 035001
Liu J.-F., Zhu J.-P., Liu L.-D., Yu Y.-W., Zhang B., 2022, ApJ, 935, L34
Lyman J. D., Galbany L., Sánchez S. F., Anderson J. P., Kuncarayakti H., Prieto J. L., 2020, MNRAS, 495, 992
Maguire K., Eracleous M., Jonker P. G., MacLeod M., Rosswog S., 2020, Space Sci. Rev., 216, 39
Margutti R. et al., 2019, ApJ, 872, 18
Metzger B. D., 2022, ApJ, 932, 84
Michałowski M. J. et al., 2019, A&A, 627, A106
Mohan P., An T., Yang J., 2020, ApJ, 888, L24

---

[10] http://www.astropy.org

Morokuma-Matsui K. et al., 2019, ApJ, 879, L13
Mummery A., 2021, preprint (arXiv:2104.06212)
Mummery A., Balbus S. A., 2020, MNRAS, 492, 5655
Mummery A., van Velzen S., Nathan E., Ingram A., Hammerstein E., Fraser-Taliente L., Balbus S., 2023, preprint (arXiv:2308.08255)
Pasham D. R. et al., 2021, Nat. Astron., 6, 249
Pellegrino C. et al., 2022, ApJ, 926, 125
Perley D. A. et al., 2019, MNRAS, 484, 1031
Perley D. A. et al., 2021, MNRAS, 508, 5138
Planck Collaboration XIII 2016, A&A, 594, A13
Predehl P. et al., 2021, A&A, 647, A1
Prentice S. J. et al., 2018, ApJ, 865, L3
Pursiainen M. et al., 2018, MNRAS, 481, 894
Rivera Sandoval L. E., Maccarone T. J., Corsi A., Brown P. J., Pooley D., Wheeler J. C., 2018, MNRAS, 480, L146
Rodrigo C., Solano E., 2020, XIV.0 Scientific Meeting (virtual) of the Spanish Astronomical Society, 182
Rodrigo C., Solano E., Bayo A., 2012, SVO Filter Profile Service Version 1.0, IVOA Working Draft 15 October 2012
Roth N., Rossi E. M., Krolik J., Piran T., Mockler B., Kasen D., 2020, Space Sci. Rev., 216, 114
Roychowdhury S., Arabsalmani M., Kanekar N., 2019, MNRAS, 485, L93
Schlafly E. F., Finkbeiner D. P., 2011, ApJ, 737, 103
Shappee B. J. et al., 2014, ApJ, 788, 48
Stanway E. R., Eldridge J. J., 2018, MNRAS, 479, 75
Stone N. C., Metzger B. D., 2016, MNRAS, 455, 859
Sun N.-C., Maund J. R., Crowther P. A., Liu L.-D., 2022, MNRAS, 512, L66
Sun N.-C., Maund J. R., Shao Y., Janiak I. A., 2023, MNRAS, 519, 3785
Tampo Y. et al., 2020, ApJ, 894, 27
Tody D., 1986, in Crawford D. L.ed., Proc. SPIE Conf. Ser. Vol. 627, Instrumentation in Astronomy VI. SPIE, Bellingham, p. 733
Tody D., 1993, in Hanisch R. J., Brissenden R. J. V., Barnes J., eds, ASP Conf. Ser. Vol. 52, Astronomical Data Analysis Software and Systems II. Astron. Soc. Pac., San Francisco, p. 173
Tonry J. L., 2011, PASP, 123, 58
van Velzen S., Stone N. C., Metzger B. D., Gezari S., Brown T. M., Fruchter A. S., 2019, ApJ, 878, 82
Virtanen P. et al., 2020, Nat. Methods, 17, 261
Wen S., Jonker P. G., Stone N. C., Van Velzen S., Zabludoff A. I., 2023, MNRAS, 522, 1155
Whitesides L. et al., 2017, ApJ, 851, 107
Xiang D. et al., 2021, ApJ, 910, 42
Yao Y. et al., 2022, ApJ, 934, 104
Zhang W. et al., 2022, Res. Astron. Astrophys., 22, 125016

APPENDIX A: BACKGROUND REGIONS

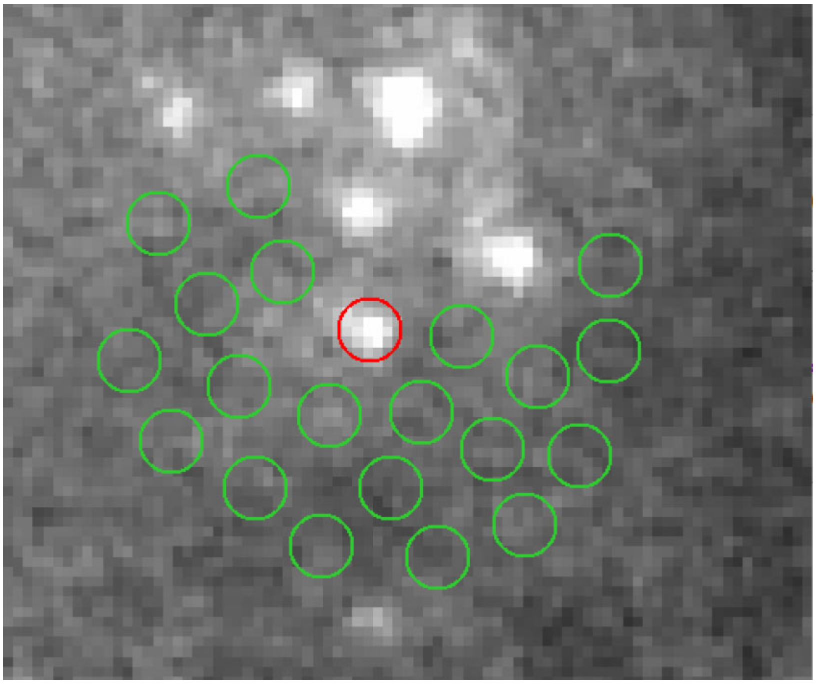

Figure A1. Grey scale F555W $T = 713$ d image showing 20 background apertures (green) placed randomly within a distance of 30 pixels from the position of AT 2018cow, shown here in red. The background apertures are placed such to avoid bright sources in the image.

APPENDIX B: ASTROMETRY SOURCES

Table B1. Coordinates of the 10 sources used to test the alignment between the epoch 1 F336W image and the epoch 3 F555W image in Section 3.1.

Source ID	RA (dd:mm:ss.ss)	Dec (dd:mm:ss.ss)
1	16:16:00.9	+ 22:16:10.8
2	16:16:00.8	+ 22:16:10.4
3	16:16:00.6	+ 22:16:08.2
4	16:16:00.9	+ 22:16:08.9
5	16:16:00.2	+ 22:16:09.2
6	16:16:00.0	+ 22:16:03.7
7	16:16:00.2	+ 22:16:05.8
8	16:16:00.2	+ 22:16:06.3
9	16:16:00.4	+ 22:16:04.2
10	16:15:59.8	+ 22:15:59.2

APPENDIX C: SED FITTING RESULTS

Here, we provide the results of age and extinction SED fitting to UV-selected compact star-forming regions, using BPASS synthetic spectra, as described in Section 3.4. In Table C1, we provide the region ID, R.A. and Dec., best-fitting age, best-fitting extinction, and reduced χ^2, where we have 4 data points and 2 parameters yielding 2 degrees of freedom.

Table C1. Results from the SED fitting procedure described in Section 3.4. Ages are spread logarithmically from 1 Myr to 100 Gyr and the extinction $A_{\rm V}$ is allowed to vary between 0 and 1 in steps of 0.1. The best-fitting age and extinction for each UV-selected star-forming region, and the reduced χ^2 of the fit, are provided. Results for the location of AT 2018cow (region 4) are provided in the first two rows at 713 and 1474 d, respectively.

Region ID	RA (hh:mm:ss.ss)	Dec (dd:mm:ss.ss)	F225W	F336W	F555W	F814W	Age/Myr	$A_{\rm V}$	χ^2_ν
Cow (713d)	16:16:00.2	+ 22:16:04.8	23.73 ± 0.05	24.05 ± 0.04	24.92 ± 0.04	24.97 ± 0.09	1.0	0.0	47.0
Cow (1474d)	16:16:00.2	+ 22:16:04.8	24.28 ± 0.06	24.44 ± 0.04	25.15 ± 0.05	25.24 ± 0.07	1.0	0.0	37.4
0	16:16:00.2	+ 22:16:06.3	24.74 ± 0.09	24.91 ± 0.07	24.99 ± 0.05	25.08 ± 0.1	8.0	0.1	0.2
1	16:16:00.2	+ 22:16:05.8	25.18 ± 0.13	24.81 ± 0.07	24.81 ± 0.04	24.46 ± 0.06	10.0	0.3	3.2
2	16:16:00.1	+ 22:16:05.7	25.63 ± 0.17	25.26 ± 0.09	25.66 ± 0.06	25.33 ± 0.1	10.0	0.1	11.8
3	16:16:00.2	+ 22:16:05.3	25.24 ± 0.17	24.91 ± 0.08	24.42 ± 0.03	23.84 ± 0.04	13.0	0.6	3.1
5	16:16:00.3	+ 22:16:03.6	24.01 ± 0.08	23.67 ± 0.05	23.42 ± 0.02	22.99 ± 0.02	13.0	0.4	1.8
6	16:16:00.3	+ 22:16:03.	25.44 ± 0.16	25.52 ± 0.12	25.76 ± 0.07	25.88 ± 0.14	8.0	0.0	0.9
7	16:16:00.5	+ 22:16:16.6	25.72 ± 0.21	25.54 ± 0.12	25.31 ± 0.06	24.85 ± 0.08	12.6	0.3	0.9
8	16:16:00.45	+ 22:16:16.5	25.71 ± 0.20	25.87 ± 0.15	25.52 ± 0.06	25.07 ± 0.08	12.6	0.3	1.6
9	16:16:01.1	+ 22:16:16.4	25.31 ± 0.15	24.91 ± 0.08	25.25 ± 0.05	24.98 ± 0.08	10.0	0.1	10.8
10	16:16:01.0	+ 22:16:16.3	25.11 ± 0.12	24.88 ± 0.07	25.24 ± 0.05	25.68 ± 0.12	1.3	0.4	2.8
11	16:16:00.4	+ 22:16:15.1	26.09 ± 0.26	25.60 ± 0.11	25.99 ± 0.07	25.55 ± 0.11	10.0	0.1	7.7
12	16:16:00.2	+ 22:16:13.3	25.91 ± 0.23	25.76 ± 0.13	25.64 ± 0.07	25.02 ± 0.09	12.6	0.3	3.8
13	16:16:00.9	+ 22:16:12.2	26.01 ± 0.23	25.50 ± 0.11	26.08 ± 0.09	26.69 ± 0.30	1.3	0.4	3.6
14	16:16:00.1	+ 22:16:11.2	25.50 ± 0.16	24.93 ± 0.08	25.30 ± 0.05	25.30 ± 0.09	7.9	0.2	10.6
15	16:16:01.0	+ 22:16:10.7	25.49 ± 0.18	24.92 ± 0.08	24.64 ± 0.04	24.51 ± 0.06	8.0	0.7	0.5
16	16:16:00.8	+ 22:16:10.4	24.77 ± 0.10	24.74 ± 0.07	24.89 ± 0.04	24.87 ± 0.07	7.9	0.2	3.0
17	16:16:00.3	+ 22:16:09.4	25.50 ± 0.18	24.93 ± 0.09	25.46 ± 0.06	26.45 ± 0.25	1.3	0.4	6.4
18	16:16:01.0	+ 22:16:08.8	25.34 ± 0.16	24.86 ± 0.08	25.03 ± 0.05	24.79 ± 0.08	10.0	0.2	6.3
19	16:16:00.5	+ 22:16:08.1	25.78 ± 0.20	25.55 ± 0.11	25.55 ± 0.08	25.80 ± 0.21	6.3	0.4	0.2
20	16:16:01.2	+ 22:16:03.2	24.22 ± 0.08	24.19 ± 0.06	24.35 ± 0.03	24.27 ± 0.05	10.0	0.0	6.6
21	16:16:01.2	+ 22:16:03.0	25.74 ± 0.20	25.54 ± 0.12	25.46 ± 0.06	25.22 ± 0.10	10.0	0.2	0.6
22	16:16:00.7	+ 22:16:00.9	26.18 ± 0.29	25.58 ± 0.12	25.69 ± 0.06	25.14 ± 0.08	12.6	0.3	5.5
23	16:16:00.5	+ 22:16:00.4	25.48 ± 0.17	25.40 ± 0.11	25.34 ± 0.05	25.34 ± 0.09	7.9	0.3	0.2

This paper has been typeset from a TEX/LATEX file prepared by the author.